

A Study of the Compact Water Vapor Radiometer for Phase Calibration of the Karl G. Jansky Very Large Array

Ajay Gill^{1,2}, Robert J. Selina³, Bryan J. Butler³

¹*National Radio Astronomy Observatory Graduate Summer Student, 1003 Lopezville Road, Socorro, NM, 87801, USA*

²*Department of Astronomy and Astrophysics, University of Toronto, Toronto, ON, M5S 3H4, Canada*

³*National Radio Astronomy Observatory, 1003 Lopezville Road, Socorro, NM, 87801, USA*

Received (to be inserted by publisher); Revised (to be inserted by publisher); Accepted (to be inserted by publisher);

We report on laboratory test results of the Compact Water Vapor Radiometer (CWVR) prototype for the NSF's Karl G. Jansky Very Large Array (VLA), a five-channel design centered around the 22 GHz water vapor line. Fluctuations in precipitable water vapor cause fluctuations in atmospheric brightness emission, T_B , which are assumed to be proportional to phase fluctuations of the astronomical signal, $\Delta\phi_V$, seen by an antenna. Water vapor radiometry consists of using a radiometer to measure variations in T_B to correct for $\Delta\phi_V$. The CWVR channel isolation requirement of < -20 dB is met, indicating $< 1\%$ power leakage between any two channels. Gain stability tests indicate that Channel 1 needs repair, and that the fluctuations in output counts for Channel 2 to 5 are negatively correlated to the CWVR enclosure ambient temperature, with a change of ~ 405 counts per 1° C change in temperature. With temperature correction, the single channel and channel difference gain stability is $< 2 \times 10^{-4}$, and the observable gain stability is $< 2.5 \times 10^{-4}$ over $\tau = 2.5 - 10^3$ sec, all of which meet the requirements. Overall, the test results indicate that the CWVR meets specifications for dynamic range, channel isolation, and gain stability to be tested on an antenna. Future work consists of building more CWVRs and testing the phase correlations on the VLA antennas to evaluate the use of WVR for not only the VLA, but also the Next Generation Very Large Array (ngVLA).

Keywords: Water vapor radiometry, phase calibration, Very Large Array, Next Generation Very Large Array, radio astronomy instrumentation

1. Background

1.1. Phase fluctuations

The prospect of water vapor radiometry (WVR) for correcting atmospheric phase fluctuations has long been recognized by the radio astronomy community. ALMA relies on radiometry of the 183 GHz water vapor line for observations at high frequencies (Sterling *et al.*, 2004). The expanded bandwidth of the NSF's Karl G. Jansky Very Large Array (VLA) receivers and recent technological developments improve the prospects of WVR corrections for phase calibration for the VLA. Successful use of WVR for phase calibration at the VLA would also be a useful case study for using WVR corrections for the Next Generation Very Large Array (ngVLA).

The troposphere is the lowest layer of the atmosphere, extending from the ground to an elevation of 7 to 10 km. The clouds and precipitable water vapor (PWV) move across the troposphere at $v_V \sim 10$ m/s, leading to a time and frequency varying refractive index, $n_V(\nu, t)$, in the layer. Planar radio wavefronts propagating through regions of $n_V(\nu, t)$ undergo refraction and an excess in electrical path length, leading to fluctuations of the phase of the wavefronts seen by an antenna, as shown in Figure 1.

The phase fluctuations due to PWV limit the spatial resolution of radio interferometers (Sutton & Hueckstaedt, 1997). The total excess path length through the atmosphere can be estimated to be (Thomp-

¹Corresponding author: Ajay Gill (ajay.gill@mail.utoronto.ca) was a summer student at the National Radio Astronomy Observatory.

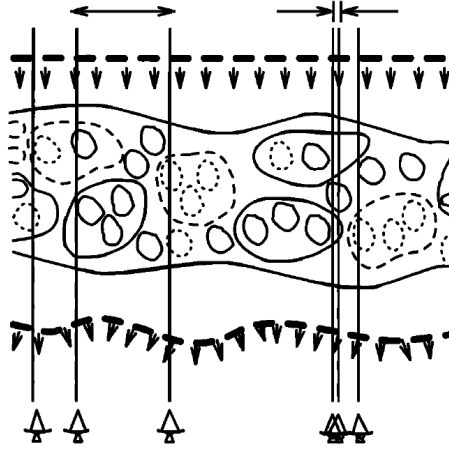


Fig. 1. Phase fluctuations due to variations in the index of refraction $n_V(\nu, t)$ (Desai, 1993).

son *et al.*, 2001)

$$\mathcal{L} \simeq \mathcal{L}_D + \mathcal{L}_V \simeq 0.228P_0 + 6.3w \quad (1)$$

where $\mathcal{L}_{D,V}$ is the excess path length due to dry air and PWV respectively, P_0 is the atmospheric pressure in millibars, and w is the height of the column of water condensed from the atmosphere. We assume P_0 and \mathcal{L}_D are slowly varying, and that the primary cause of phase fluctuations is \mathcal{L}_V . PWV of extent w causes a phase change of the incoming radio wave, $\Delta\phi_V$, as (Butler, 1999)

$$\Delta\phi_V \simeq \frac{12.6\pi}{\lambda} \times w \quad (2)$$

A plot of the optical depth at the VLA site with $w = 4$ mm is shown in Figure 2. Below 130 GHz, both O_2 and H_2O contribute to the optical depth, whereas H_2O primarily contributes to the optical depth above 130 GHz.

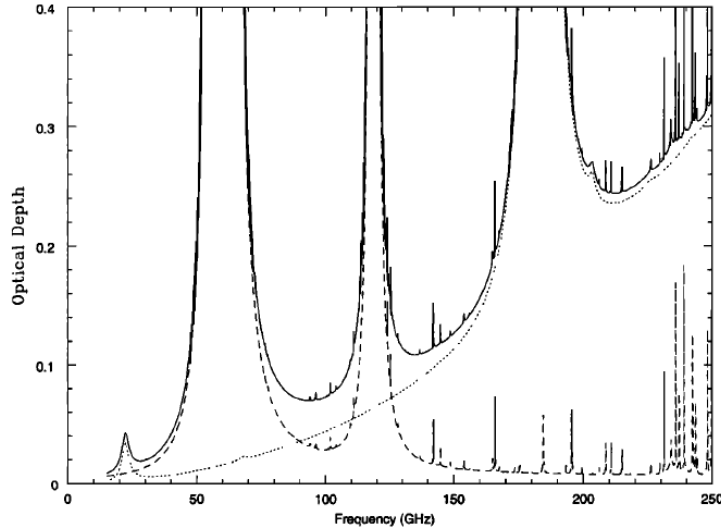


Fig. 2. Optical depth at the EVLA site with $w = 4$ mm. The dotted line is the optical depth due to water vapor. The dashed line is the optical depth due to dry air (O_2 & other trace gases). The solid line is the total optical depth (Carilli & Holdaway, 1999).

1.2. Techniques for phase correction

The various techniques used for phase calibration are briefly discussed below.

- (1) *Self calibration* - The target source itself can be used for phase correction if it at least has a signal-to-noise ratio of ~ 2 over the self-calibration averaging time (Cornwell & Fomalont, 1999). This technique is not possible for weaker continuum or spectral line sources.
- (2) *Fast switching* - This technique consists of observing a strong calibrator source with a calibration cycle time short enough to reduce atmospheric phase fluctuations (Fomalont & Perley, 1999; Holdaway & Owen, 1995). Fast switching decreases observation time on the target source and places stringent constraints on the slew rate and mechanical settling time of the antenna.
- (3) *Paired array* - This technique uses a separate array that observes a nearby calibrator source while the target array continuously observes the target source (Holdaway, 1992). Paired elements constrain array configuration and reduce the sensitivity of the interferometer by a factor of 1.5 - 2 (Clark, 2015).
- (4) *Water vapor radiometry* - Fluctuations in PWV cause fluctuations in atmospheric brightness emission, T_B , which are assumed to be proportional to phase fluctuations of the astronomical signal, $\Delta\phi_V$. WVR consists of using a radiometer to measure variations in T_B to correct for $\Delta\phi_V$ (Lay, 1997). WVR must be able to work well consistently under a variety of weather conditions.

1.3. Liquid water

A complication arises for WVR because liquid and frozen water are also sources of continuum emission ($T_B \propto \nu^2$) but have a minimal contribution to the excess electrical path length. Therefore, water vapor emission may not correlate well with the astronomical phase fluctuations in the presence of liquid water, presenting a challenge for continuum radiometry.

Water vapor emits both line and continuum emission. To distinguish water vapor emission from liquid water emission, one of the water vapor lines (22 or 183 GHz) can be observed with multiple channels around the line. One of the channels should be away from the water vapor emission line to distinguish the ν^2 continuum of liquid water from the vapor. WVR can be achieved in two ways: absolute and empirical radiometric phase correction.

1.4. Absolute radiometric phase correction

The brightness temperature due to atmospheric emission can be given by the radiometry equation as (Dicke *et al.*, 1946)

$$T_B = T_{atm}(1 - e^{-\tau_{tot}}) \quad (3)$$

where T_{atm} is the physical temperature of the atmosphere, and τ_{tot} is the total optical depth, which depends on dry air and water vapor. We assume τ_{tot} can be separated into three parts (Carilli & Holdaway, 1999)

$$\tau_{tot} = A_\nu w_o + B_\nu + A_\nu w_{rms} \quad (4)$$

where A_ν is the optical depth per mm of PWV as a function of frequency, w_o is the temporally stable component of PWV, B_ν is the temporally stable optical depth due to dry air as a function of frequency, and w_{rms} is the time-varying component of PWV. We assume a temporally stable optical depth term, $\tau_o \equiv A_\nu w_o + B_\nu$, and a time-varying optical depth term, $\tau_{rms} \equiv A_\nu w_{rms}$, and that $\tau_o \gg \tau_{rms}$. Inserting equation 4 into 3 and assuming $\tau_{rms} \ll 1$ yields

$$T_B = T_{atm}(1 - e^{-\tau_o}) + T_{atm}e^{-\tau_o} \left[A_\nu w_{rms} - \frac{(A_\nu w_{rms})^2}{2} + \dots \right] \quad (5)$$

The first term in equation 5 represents the temporally stable non-varying T_B , and the second term represents the fluctuating component due to variations in PWV, which to first-order reduces to

$$T_B^{rms} = T_{atm}e^{-\tau_o} A_\nu w_{rms} \quad (6)$$

Absolute radiometric phase correction consists of measuring T_B^{rms} using a radiometer, inverting equation 6 to derive the fluctuation in PWV, w_{rms} , and using equation 2 to infer and correct for the fluctuation in phase, $\Delta\phi_V$, along the line of sight. However, there are some uncertainties involved with using absolute radiometry. The above derivations presume that the PWV fluctuations occur in a single narrow layer of known height, h_{turb} , that remains constant over time. If the PWV fluctuations are instead distributed over a large range of altitudes, then the height of the dominant fluctuation at any given time must be known to convert T_B^{rms} into $\Delta\phi_V$. If PWV fluctuations at different heights contribute to T_B^{rms} simultaneously, the conversion becomes inaccurate. Another uncertainty in making absolute radiometric corrections involves errors in the theoretical atmospheric models that relate w to T_B .

1.5. Empirical radiometric phase correction

Absolute radiometric phase correction at each antenna places stringent requirements on the accuracy of the measured T_B , ancillary data (T_{atm} , h_{turb} , etc.), and of the theoretical atmospheric models. A way to avoid some of these uncertainties is to empirically calculate the correlation between T_B^{rms} and $\Delta\phi_V$ by observing a strong calibration source at regular intervals. The phase fluctuation is a differential measurement between the phase, ϕ , of antennas i and j of a single baseline taken as (Chandler *et al.*, 2004a)

$$\Delta\phi_V = \phi_i - \phi_j \quad (7)$$

The brightness emission fluctuation, $T_B^{rms} \equiv \Delta T_B$, to be compared with $\Delta\phi_V$ is also a differential measurement between the *observable*, ΔT , of antennas i and j of the same baseline taken as

$$\Delta T_B = \Delta T_i - \Delta T_j \quad (8)$$

The scaling factor derived from the correlation between ΔT_B and $\Delta\phi_V$ can then be used to correct for $\Delta\phi_V$. Empirical radiometry consists of finding correlations between ΔT_B and $\Delta\phi_V$ for every baseline, so each antenna in the array requires a WVR. For preliminary tests with a single baseline, a minimum of two WVRs are required to test for correlations. A minimum of three WVRs are required to determine phase closure errors.

2. Prior water vapor radiometers

A three-channel WVR was tested on VLA antennas 26 and 28 for one year as described in (Chandler *et al.*, 2004b). The 183 GHz line at the VLA site is too saturated, so the 22 GHz line was used. The block diagram of the VLA WVR is shown in Figure 3.

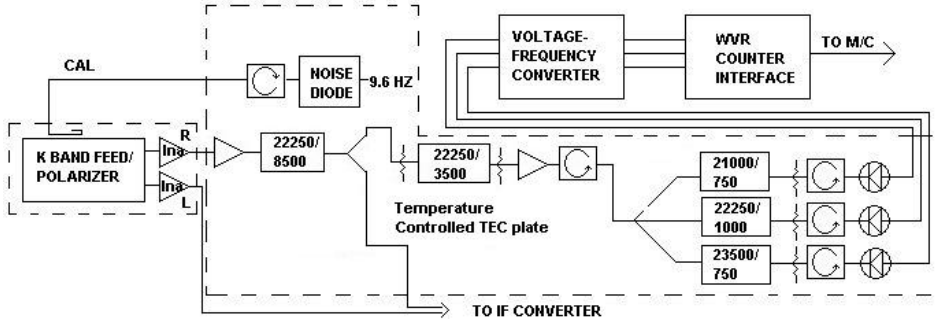


Fig. 3. VLA water vapor radiometer block diagram (Chandler *et al.*, 2004b).

The channels were placed at $\nu_1 = 21.00$ GHz with $\Delta\nu_1 = 750.00$ MHz, $\nu_2 = 22.25$ GHz with $\Delta\nu_2 = 1000.00$ MHz, and $\nu_3 = 23.50$ GHz with $\Delta\nu_3 = 750.00$ MHz. The *observable*, ΔT , per antenna was defined as

$$\Delta T = w_1 T_1 + w_2 T_2 + w_3 T_3 \quad (9)$$

where the weights were $w_1 = -0.5$, $w_2 = 1.0$, and $w_3 = -0.5$, and T_1 , T_2 , and T_3 were the brightness temperatures of the three channels. The location of the channels is shown in Figure 4.

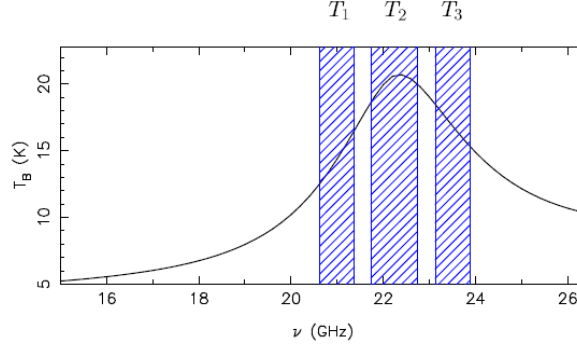


Fig. 4. Three channels of the VLA water vapor radiometer (Chandler *et al.*, 2004b).

For $\sim 35 \mu\text{m}$ of PWV, an excess path length $\mathcal{L}_V \sim 220 \mu\text{m}$ or $(\lambda/30$ for $\lambda = 7 \text{ mm})$ was predicted from equation 1. By considering possible atmospheric models and the channel locations, it was predicted that $\sim 35 \mu\text{m}$ of PWV would result in $\Delta T \sim 25 \text{ mK}$. For an observable $\Delta T_{rms} \sim 25 \text{ mK}$ with the chosen weights, the stability of an individual channel needed to be $\sim 20 \text{ mK}$. For typical system temperatures of 50 - 100 K, this implied a gain stability $\Delta g/g \sim 2 - 4 \times 10^{-4}$. Test results showed that the sensitivity and gain stability requirements of the WVRs were met. The astronomical phase on baseline 26 - 28 was most significantly improved when the sky was clear and the phase fluctuations were large. Phase residuals were not significantly improved in the presence of clouds or when phase fluctuations were small.

3. Compact water vapor radiometer

3.1. Motivation

The prior WVRs were designed for the VLA rather than the Expanded Very Large Array (EVLA). The K-band for the VLA had a frequency range from 21.40 - 24.40 GHz, so the VLA WVRs were limited to three channels because of the narrow 3.00 GHz bandwidth. The K-band for the EVLA has a frequency range of 18.00 - 26.50 GHz with a bandwidth of 8.50 GHz, so a five-channel compact water vapor radiometer (CWVR) was proposed, designed, and built. The five-channel CWVR improves the ability to distinguish liquid water from water vapor. The CWVR is based on Monolithic Microwave Integrated Circuit (MMIC) technology instead of discrete components, and its smaller size makes it easier to fit inside the space available in the vertex room of the antenna.

3.2. CWVR system overview

3.2.1. Block diagram

The block diagram of the CWVR is shown in Figure 5. Major elements of the diagram are described in the following sections.

3.2.2. K-band Dewar

The astronomical signals arrive at the feed horn of the K-band receiver. The signals pass through a 90° phase shifter, which converts the two linear orthogonal polarizations into two circular polarizations. The two circular polarizations are then split into right-hand circularly polarized (RCP) and left-hand circularly

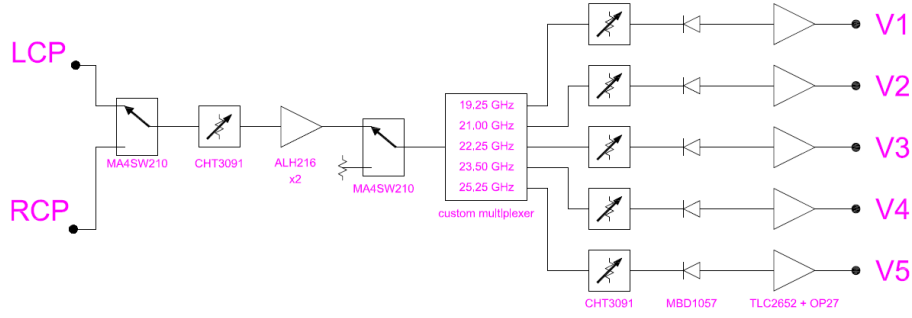


Fig. 6. Block diagram of the MMIC block.

3.2.4. MMIC block

The block diagram of the MMIC block is shown in Figure 6. An input MA4SW210 PIN diode switch can select between the LCP and RCP input signals. The signal then passes through a CHT3091, which is a 100 step variable digital attenuator. The signal is amplified again by an ALH216 amplifier. The second MA4SW210 PIN diode switch can select between the incoming LCP/RCP signals and a termination to ground. The termination to ground allows DC offsets in the post-amps and diode detectors to be measured. The signal is then multiplexed with a frequency multiplexer into the 5 channels given in Table 1 and Figure 7.

Table 1. Location of the 5 CWVR channels.

| Channel | ν_{low} (GHz) | ν_{center} (GHz) | ν_{high} (GHz) | $\Delta\nu$ (GHz) |
|---------|----------------------|-------------------------|-----------------------|----------------------|
| 1 | 18.500 | 19.250 | 20.000 | 1.500 |
| 2 | 20.625 | 21.000 | 21.375 | 0.750 |
| 3 | 21.750 | 22.250 | 22.750 | 1.000 |
| 4 | 23.125 | 23.500 | 23.875 | 0.750 |
| 5 | 24.500 | 25.250 | 26.000 | 1.500 |

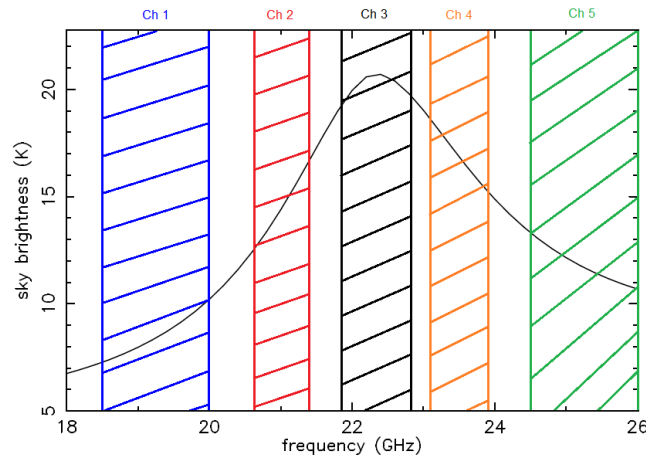


Fig. 7. Five channels of the CWVR.

The DC offset counts were measured for a period of 90 minutes, and the median values per channel

are given in Table 2.

Table 2. Median DC offset counts per channel.

| | Ch 1 | Ch 2 | Ch 3 | Ch 4 | Ch 5 |
|--------------------|------|------|------|------|------|
| Mean offset counts | 272 | 270 | 296 | 235 | 207 |

The signal then goes through another CHT3091 attenuator per channel. The attenuators in the MMIC block are controlled through the function control box with a DB25 cable. Then, the signal goes to a MBD1057 tunnel diode detector, with the detector voltage output amplified by TLC2652 and OP27 amplifiers. The 0 - 10 V output from the amplifiers, proportional to the input RF power per channel, is then sent to the Voltage to Frequency board.

3.2.5. Voltage to Frequency board

The 0 - 10V output per channel from the MMIC block is sent to a Voltage to Frequency (V-F) Converter (VFC110AP), which converts the 0 - 10 V voltage inputs to 0 - 2 MHz frequency outputs. The frequency outputs of the five channels are sent to the F318 module using ST-E2000 fiber optic cables.

3.2.6. F318 module

The block diagram of the F318 module is shown in Figure 8. The F318 module is required to interface the EVLA monitor and control system to the fiber optic cables of the five channel CWVR. The F318 also monitors temperatures within the CWVR. Figure 8 shows the main boards of the module. The Analog to Digital Interface Board brings in a total of twenty-nine analog voltages through four input channels. The F318 MIB Interface Board is the primary interface between the MIB and the CWVR, with the frequency counter implemented in the Xilinx FPGA. These two boards along with the MIB provide for a simple interface for analog and digital monitoring of the CWVR. Further details on the functionality of the F318 module with the CWVR are provided in (Koski, 2017).

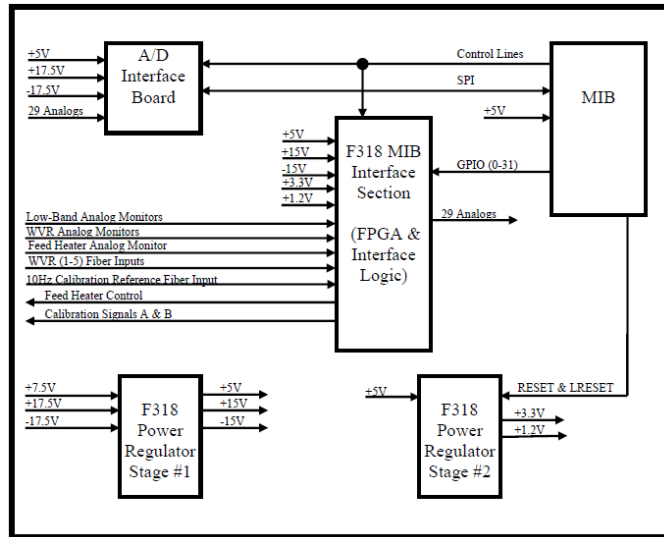


Fig. 8. F318 module block diagram (Koski, 2017).

The 10 Hz noise diode calibration signal, with a period of 100 ms and 50% duty cycle, is used to count the number of pulses every high and low cal cycle. The data is collected every 100 ms at the rising edge of

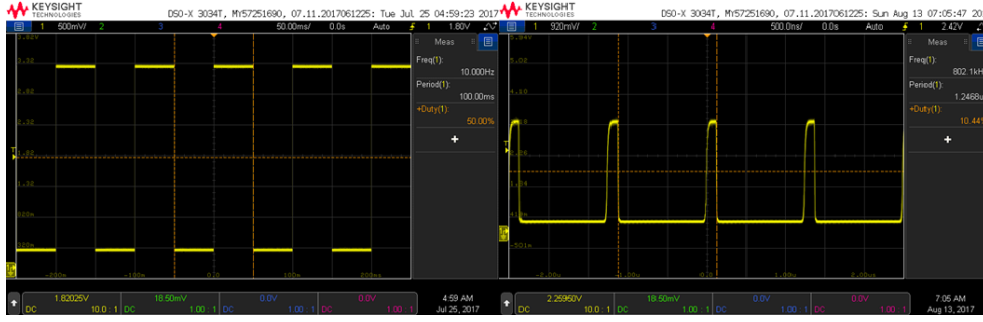


Fig. 9. 10 Hz calibration signal (left) & channel frequency output (right).

the 10 Hz signal. For the waveforms shown in Figure 9, as an example

$$Ch1_{low,high} = \frac{802.1 \times 10^3 \text{ counts}}{\text{sec}} \times 50 \text{ ms} \times \frac{1 \text{ sec}}{10^3 \text{ ms}} \simeq 40,000 \text{ counts} \quad (10)$$

$$Ch1_{total} = Ch1_{low} + Ch1_{high} \simeq 80,000 \text{ counts} \quad (11)$$

3.2.7. Temperature control

The temperature of the temperature controlled plate (TCP) on which the post-amps, filters, and the MMIC block are mounted is maintained using a CP-036 Peltier Thermoelectric Cooler (TEC). The TEC is controlled using a MPT-5000 linear, bipolar temperature controller. The MPT-5000 contains a 12 turn trimpot, which can be adjusted to set the desired temperature. The heat from the TCP is absorbed into the heat sink of the TEC, and a fan is used to remove this heat to the outside of the CWVR. For laboratory testing, the temperature of the TCP was set to 30°C to minimize reflections and losses in Teflon cables. The PID control loop employs a TCS-620 temperature sensor, which has a resistance of 20 kΩ at 25°C.

The Temperature Setpoint (TS) and Temperature Monitor (TM) signals of the MPT-5000 are used to set the temperature of the TEC and to monitor the temperature of the TCS-620, respectively. During stable operation, the voltage of TS closely matches that of TM. Two additional AD590 temperature sensors were used to monitor the temperature of the TCP adjacent to the post amps and the ambient temperature within the CWVR enclosure. Table 3 lists the signal names and descriptions of signals on the MIB for signals related to temperature control and monitor.

Table 3. Signal names on Monitor and Interface Board.

| Signal name | Description |
|-------------|--|
| WVR 7 | Temperature monitor for TCS-620 (TCP) |
| WVR 8 | Temperature setpoint for TEC |
| WVR_Temp1 | Temperature monitor for AD590 (CWVR ambient) |
| WVR_Temp2 | Temperature monitor for AD590 (TCP) |

4. Compact water vapor radiometer requirements

4.1. Channel isolation requirement

The integrated isolation between any two channels is defined as

$$IS_{xy} = \frac{\int_{\nu_i}^{\nu_f} P_x(\nu) P_y(\nu) d\nu}{\int_{\nu_i}^{\nu_f} P_y(\nu) d\nu} \quad (12)$$

where IS_{xy} is the power leakage from channel x into channel y, $\nu_i = 17.00$ GHz, $\nu_f = 27.00$ GHz, and $P_x(\nu)$ and $P_y(\nu)$ is the output power at frequency ν of channel x and y, respectively. The requirement for channel isolation IS_{xy} was specified to be < -20 dB, or a power leakage from channel x into channel y of $< 1\%$.

4.2. Gain stability requirement

From the initial stability tests, Channel 1 was measured to be defective, so it was subsequently ignored, and the gain stability requirements were set for Channels 2 to 5. For Channels 2 to 5 of the CWVR given in Table 1, the *observable*, ΔT , per antenna can be defined as

$$\Delta T \propto \Delta P_{in} = w_2 P_2 + w_3 P_3 + w_4 P_4 + w_5 P_5 \quad (13)$$

where the weights are typically $w_2 = -0.5$, $w_3 = 1.0$, $w_4 = -0.5$, $w_5 = 0.25$, and P_2 , P_3 , P_4 , and P_5 are the power outputs due to sky emission in the five channels. It can be estimated from equation 1 that $\sim 35 \mu\text{m}$ of PWV leads to $\mathcal{L}_V \sim 220 \mu\text{m}$ of excess electrical path length ($\lambda/30$ for $\lambda = 7$ mm) and will result in $\Delta T \sim 25$ mK (Butler, 1999). For $\Delta T_{rms} \sim 25$ mK, the stability of each individual channel needs to be ~ 20 mK. For typical system temperatures of 50 - 100 K, this requires a gain stability for $\Delta g/g \sim 2.5 - 5 \times 10^{-4}$ for ΔT and $\Delta g_i/g_i \sim 2 - 4 \times 10^{-4}$ for each individual channel.

The short timescale, τ_{short} , for which the CWVR needs to be gain stable is

$$\tau_{short} = \frac{D}{v_V} = \frac{25 \text{ m}}{10 \text{ m/sec}} = 2.5 \text{ sec} \quad (14)$$

where D is the diameter of the antenna and v_V is the average speed of water vapor across the troposphere. The long timescale for which the CWVR needs to be gain stable is $\tau_{long} \sim 10^3$ sec to allow for longer calibration cycles of the interferometer. The stability of the CWVR channels on different timescales, τ , was characterized by the Allan Standard Deviation (ASD), $\sigma_P(\tau)$ defined by

$$\sigma_P(\tau) = \left\{ \frac{1}{2} \langle \{P(t) - P(t - \tau)\}^2 \rangle \right\}^{\frac{1}{2}} \quad (15)$$

For single channel ASDs with N time and output power data points, equation 15 becomes

$$\sigma_P(\tau) = \left\{ \frac{1}{2} \sum_{j=1}^{N/2} \frac{1}{N - \tau_j} \sum_{i=1}^{N - \tau_j} \{P(t_i + \tau_j) - P(t_i)\}^2 \right\}^{\frac{1}{2}} \quad (16)$$

where $\sigma_P(\tau)$ is normalized with respect to

$$\mu_P = \langle P(t) \rangle \quad (17)$$

For channel difference ASDs with N time and output power data points, equation 15 becomes

$$\sigma_{P_x - P_y}(\tau) = \left\{ \frac{1}{2} \sum_{j=1}^{N/2} \frac{1}{N - \tau_j} \sum_{i=1}^{N - \tau_j} \{[P_x(t_i + \tau_j) - P_y(t_i + \tau_j)] - [P_x(t_i) - P_y(t_i)]\}^2 \right\}^{\frac{1}{2}} \quad (18)$$

where $\sigma_{P_x - P_y}(\tau)$ is normalized with respect to

$$\mu_{P_x - P_y} = \frac{\langle P_x(t) + P_y(t) \rangle}{2} \quad (19)$$

For the ASD of ΔP_{in} with N time and output power data points, equation 15 becomes

$$\sigma_{\Delta P_{in}}(\tau) = \left\{ \frac{1}{2} \sum_{j=1}^{N/2} \frac{1}{N - \tau_j} \sum_{i=1}^{N - \tau_j} \left\{ \sum_{k=2}^5 w_k P_k(t_i + \tau_j) - \sum_{k=2}^5 w_k P_k(t_i) \right\}^2 \right\}^{\frac{1}{2}} \quad (20)$$

where $\sigma_{\Delta P_{in}}(\tau)$ is normalized with respect to

$$\mu_{\Delta P_{in}} = \frac{\langle P_2(t) + P_3(t) + P_4(t) + P_5(t) \rangle}{4} \quad (21)$$

4.3. Temperature stability requirement

Since the temperature coefficients of the CWVR components were not established prior to these tests, the physical temperature stability requirement inside the CWVR and on the TCP was arbitrarily set to ~ 25 mK over 10^3 sec timescales.

5. Results

5.1. Dynamic range

The dynamic range of the MBD1057 tunnel diode detectors was determined by sending input continuous wave power at the center of each channel at power levels ranging from -90 to -30 dbm. The resulting plot of output counts versus input power level per channel is shown in Figure 10. At -90 dbm input, the channels are at the noise floor. Channel 5 has the highest noise floor possibly due to its wider than desired design bandwidth.

As the input power increases, the counts increase and approach the linear region labeled *square law*. In the square-law region, $\Delta T \propto \Delta P_{in} \propto V_{out} \propto Counts_{out}$. The CWVR should be operated in the square-law region, as it is in this region that the output counts are most sensitive to changes in input power. The square-law region ranges from ~ -58 to -52 dbm, providing a dynamic range of ~ 6 dbm. At input powers above -52 dbm, the diode detectors go into saturation.

In the region labeled *fit* ranging from -90 to -52 dbm, the curve for each channel was fit to the form given in equation 22 to find the relationship between counts and input power. The fit effectively increases the dynamic range of the detectors to ~ 18 dbm.

$$P_{in}(dbm) = \frac{1}{A} \{ \ln(Counts) - \ln(B) \} \quad (22)$$

where the constants A and B per channel are given in Table 4.

Table 4. Constants per channel for equation 22.

| | A | B |
|------|-------|------------------------|
| Ch 1 | 0.225 | 1.518×10^{10} |
| Ch 2 | 0.232 | 2.191×10^{10} |
| Ch 3 | 0.228 | 1.809×10^{10} |
| Ch 4 | 0.231 | 2.107×10^{10} |
| Ch 5 | 0.224 | 1.455×10^{10} |

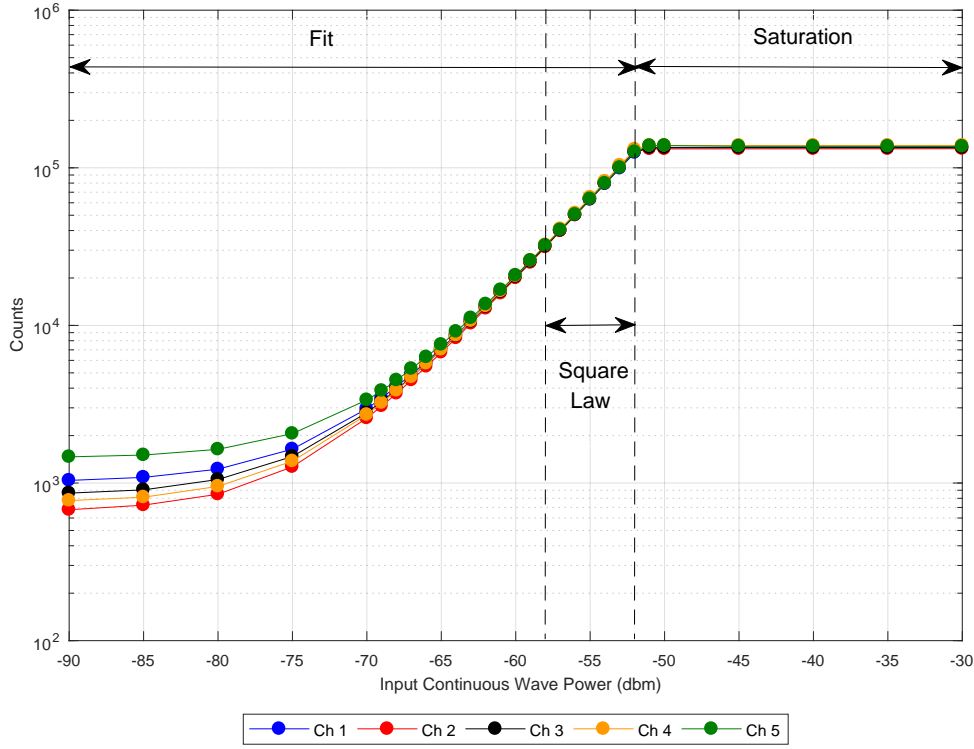


Fig. 10. Dynamic range of the diode detectors.

5.2. Channel isolation

The power response of the CWVR was measured as a function of frequency. Frequency sweeps were done from 17.00 to 27.00 GHz at ~ 6.41 MHz/sec at input power levels from -30 to -55 dbm with increments of -5 dbm. The Keysight PSG E8257D 250.00 kHz - 40.00 GHz Analog Signal Generator was used for the sweeps, and a MegaPhase RF Orange cable with a maximum operating frequency of 50.00 GHz was used to connect the generator to the CWVR input. For the sweeps, input power was sent only to the LCP input of the CWVR. The overall power response was determined by combining the unsaturated regions of the response curves at input power levels ranging from -30 to -55 dbm, and it is shown as a function of frequency in Figure 11.

Using the data in Figure 11, the isolation between all channels was calculated using equation 12 and the results are given in Table 5. All values are < -20 dB, indicating $< 1\%$ power leakage between any two channels, which meets the specification.

Table 5. Measured isolation between CWVR channels.

| $IS_{12}(dB)$ | $IS_{13}(dB)$ | $IS_{14}(dB)$ | $IS_{15}(dB)$ |
|---------------|---------------|---------------|---------------|
| -25.09 | -30.79 | -29.25 | -32.38 |
| $IS_{21}(dB)$ | $IS_{23}(dB)$ | $IS_{24}(dB)$ | $IS_{25}(dB)$ |
| -27.42 | -22.90 | -26.10 | -27.72 |
| $IS_{31}(dB)$ | $IS_{32}(dB)$ | $IS_{34}(dB)$ | $IS_{35}(dB)$ |
| -31.99 | -21.78 | -20.25 | -25.46 |
| $IS_{41}(dB)$ | $IS_{42}(dB)$ | $IS_{43}(dB)$ | $IS_{44}(dB)$ |
| -31.15 | -25.67 | -20.95 | -22.74 |
| $IS_{51}(dB)$ | $IS_{52}(dB)$ | $IS_{53}(dB)$ | $IS_{54}(dB)$ |
| -32.34 | -25.35 | -24.22 | -20.81 |

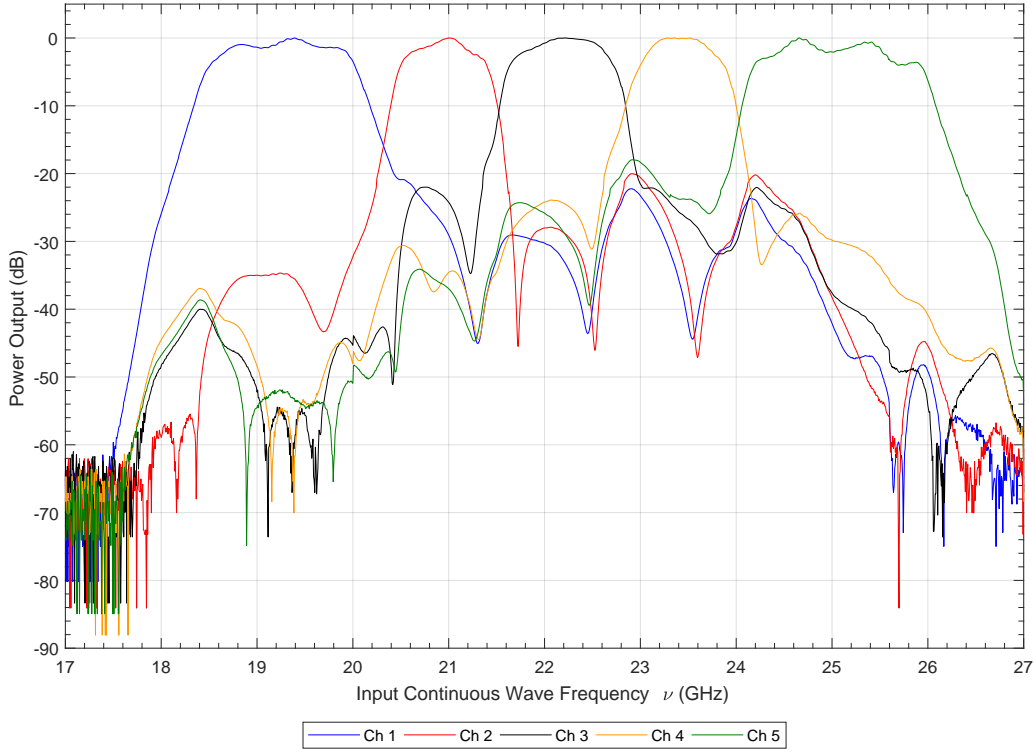


Fig. 11. Power response of the CWVR channels as a function of frequency.

5.3. Gain stability

The instrumental setup used to test the gain stability of the CWVR is shown in Figure 12. The K-band noise diode source from within the CWVR generates broadband noise from 18.00 - 26.50 GHz. The noise diode signal is taken as an output from the CWVR and is sent through a MICA T-318S20 isolator to minimize reflections. The noise diode signal with no amplification is too weak to provide output counts in the square-law region, so a K-band LNA with a gain of 35 dB was used to amplify the signal. The LNA is within the Dewar, which is cooled to ~ 6 K to minimize noise and gain fluctuations generated by the LNA itself. The output signal from the Dewar has 13 dB of attenuation before going to the LCP input of the CWVR.

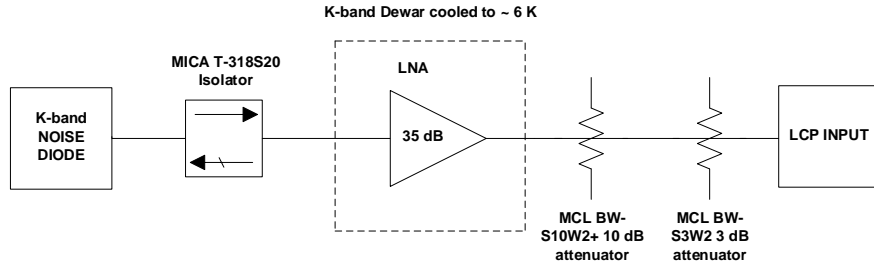


Fig. 12. Block diagram of gain stability test setup.

With the combination of the 13 dB attenuation and adjustment of the CHT3091 attenuators in the MMIC block, the output counts were set to $\sim 60,000$ counts per channel in the square-law region of the diode detectors. The test was run for a period of 64 hours, and data of the output counts per channel and the temperature sensors was collected every second.

The measured output counts per channel over the 64 hr period averaged with a 20 min running mean

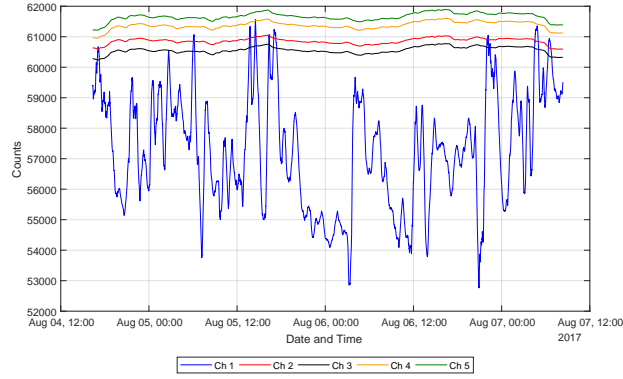


Fig. 13. Output counts of Channel 1 to 5 over 64 hrs averaged with 20 min running mean.

are shown in Figure 13. Channel 1 is much more unstable than the rest, possibly due to its attenuation varying with time, so it was subsequently ignored. The counts from Channel 2 to 5 averaged with a 20 min running mean are shown in Figure 14. There is a slight offset in counts between the channels due to the step size of the CHT3091 attenuators.

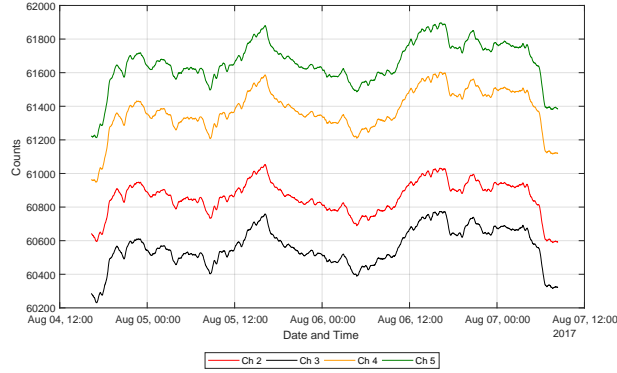


Fig. 14. Output counts of Channel 2 to 5 over 64 hrs averaged with 20 min running mean.

5.3.1. *Single channel Allan Standard Deviations*

The ASD for Channels 2 to 5 was calculated using equations 16 and 17, and the results are shown in Figure 15. The two horizontal dashed lines represent the single channel gain stability requirement of $2 - 4 \times 10^{-4}$. The two vertical lines represent the timescale $\tau = 2.5 - 10^3$ sec over which the gain stability is required. Figure 15 shows that the gain stability for Channels 2 to 5 is $< 2 \times 10^{-4}$ over $\tau = 2.5 - 10^{2.65}$ sec and within $2 - 4 \times 10^{-4}$ from $\tau = 10^{2.65} - 10^3$ sec, so an improvement from $\tau = 10^{2.65} - 10^3$ sec is desirable.

5.3.2. *Channel difference Allan Standard Deviations*

The channel difference ASDs are also calculated, as the single channel ASDs are limited by the stability of the input noise diode source and common signal path elements, whereas the difference ASDs measure the intrinsic stability of the independent signal paths. The channel difference ASDs were calculated for Channels 2 to 5 with respect to each other, and the results are shown in Figures 16, 17, 18, and 19. The results show that the gain stability of $2 - 4 \times 10^{-4}$ over $\tau = 2.5 - 10^3$ sec is successfully met for all cases.

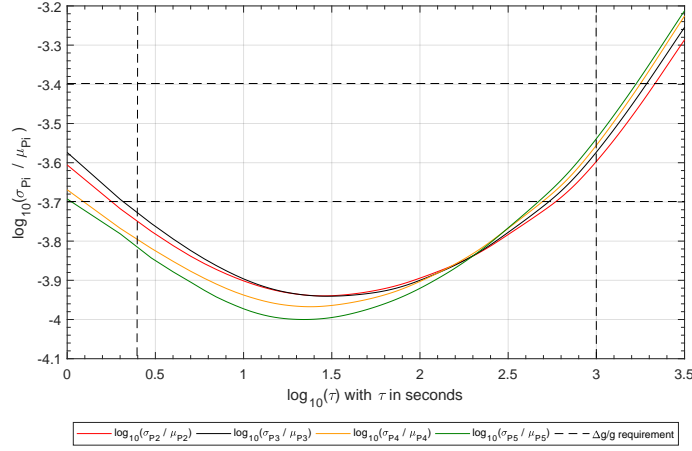


Fig. 15. Single channel Allan Standard Deviations. The two horizontal dashed lines represent single channel gain stability requirement of $2 - 4 \times 10^{-4}$. The two vertical lines represent the timescale $\tau = 2.5$ to 10^3 sec over which the gain stability is required.

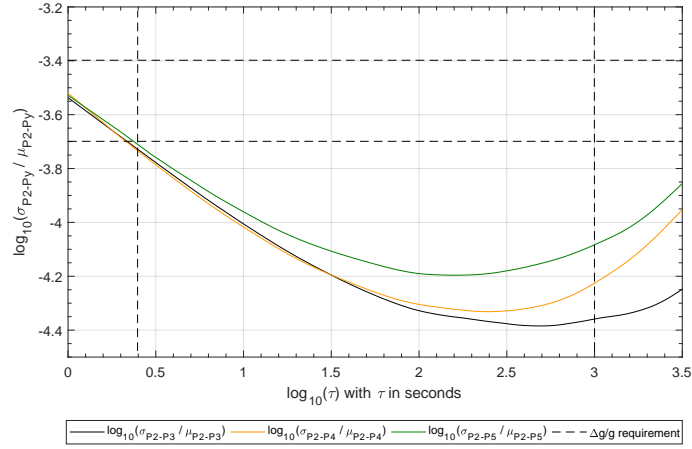


Fig. 16. Channel 2 Difference Allan Standard Deviations: Ch 2-3, Ch 2-4, and Ch 2-5.

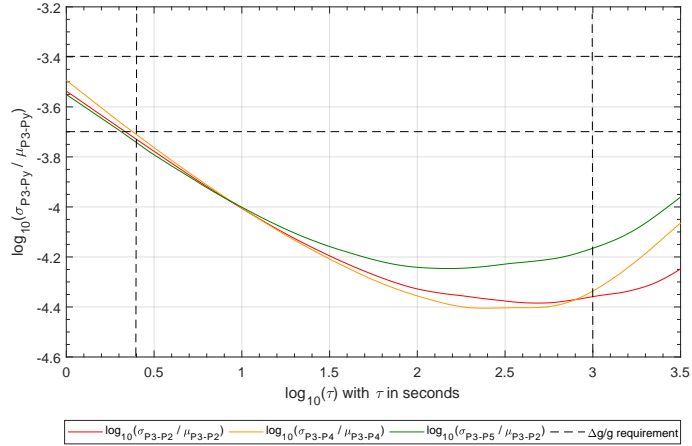


Fig. 17. Channel 3 Difference Allan Standard Deviations: Ch 3-2, Ch 3-4, and Ch 3-5.

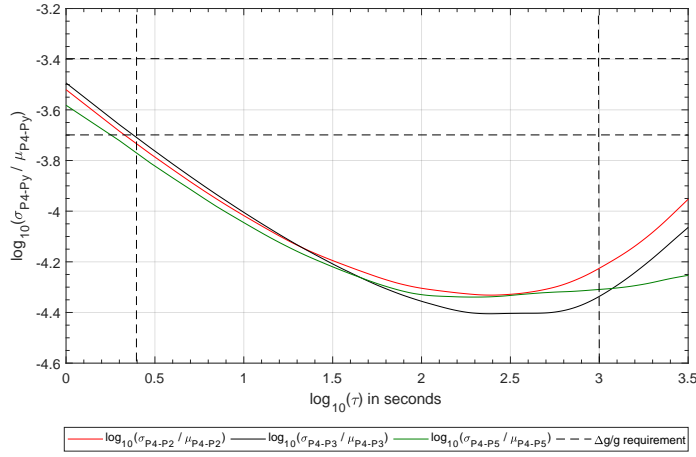


Fig. 18. Channel 4 Difference Allan Standard Deviations: Ch 4-2, Ch 4-3, and Ch 4-5.

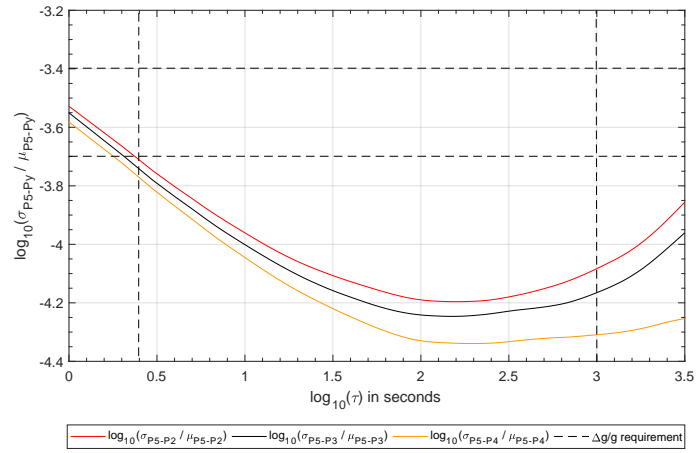
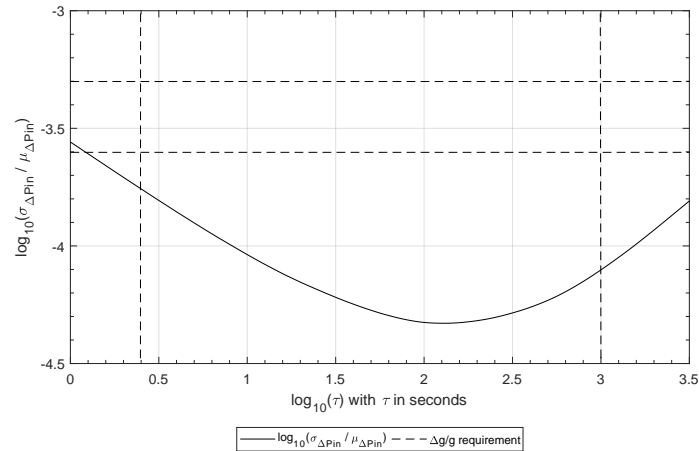


Fig. 19. Channel 5 Difference Allan Standard Deviations: Ch 5-2, Ch 5-3, and Ch 5-4.

5.3.3. Observable Allan Standard Deviation

The ASD of ΔP_{in} was calculated using equations 20 and 21, and the result is shown in Figure 20. The result shows that the gain stability requirement of $2.5 - 5 \times 10^{-4}$ over $\tau = 2.5 - 10^3$ sec is successfully met.

Fig. 20. Observable ΔP_{in} Allan Standard Deviation.

5.3.4. Temperature Allan Standard Deviations

The ASD of the three temperature sensors was calculated, and the results are shown in Figure 21. The results show that the temperature stability requirement of ~ 25 mK was met for all the thermistors. The ASD of the TCP AD590 follows that of the TCP TCS-620 on longer timescales as expected. The measuring circuit employed by the TCS620 has lower noise for short time scales, and is more representative of the true temperature stability of the TCP.

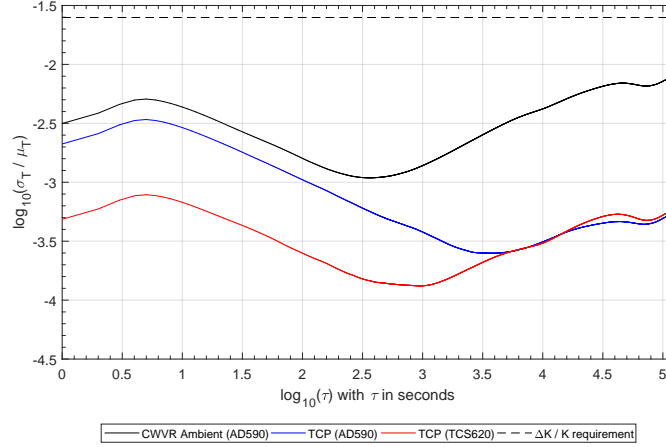


Fig. 21. Temperature Allan Standard Deviations. The horizontal dashed line is the 25 mK requirement.

5.4. Gain stability with temperature correction

5.4.1. Temperature correlation

Figure 14 shows that the large-scale fluctuations in the output counts are consistent for Channels 2 to 5, suggesting a common source of the fluctuations. The CWVR ambient temperature and Channel 2 counts averaged with a 20 min running mean are plotted as a function of time over the 64 hr period in Figure 22. It is apparent from Figure 22 that the CWVR ambient temperature and the output counts are negatively correlated.

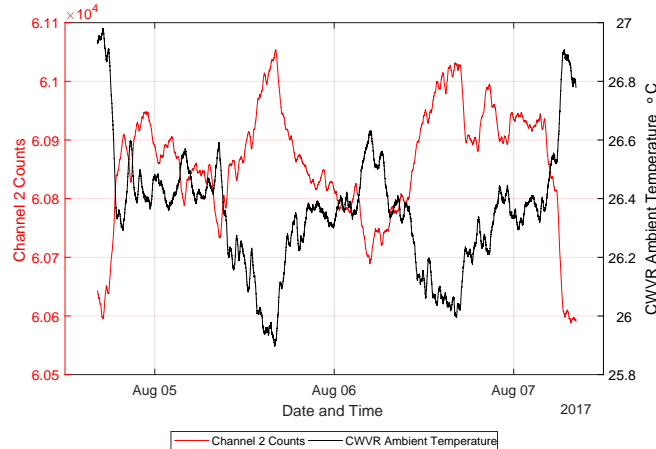


Fig. 22. Ch 2 Counts & CWVR Ambient Temperature over 64 hr period averaged with a 20 min running mean.

A scatter plot of Channel 2 counts versus CWVR ambient temperature smoothed with a 5 min running mean is shown in Figure 23. The Pearson correlation coefficient between the Channel 2 counts and the

CWVR ambient temperature is calculated to be $r = -0.83$ with 99.00% confidence. The coefficient of determination, R^2 , for the linear fit is 0.69, providing an indication of the goodness of the fit. The slope of the fit indicates a change of ~ 405 counts per 1°C change in the CWVR ambient temperature.

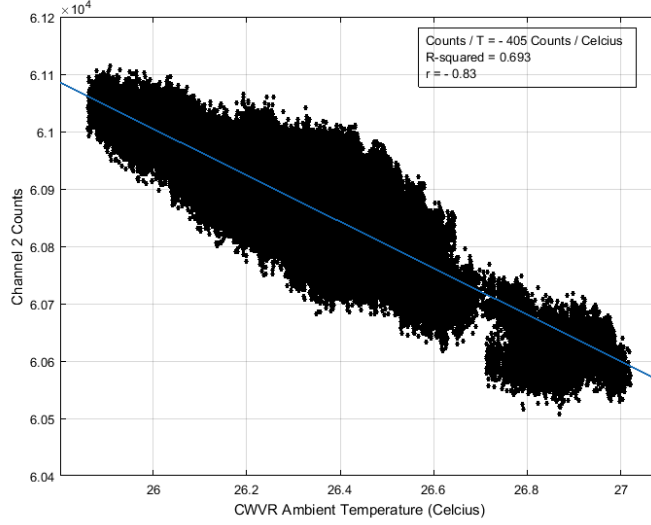


Fig. 23. Scatter plot of Channel 2 counts and CWVR ambient temperature.

5.4.2. Temperature correction

It is possible to correct for the changes in counts due to changes in the CWVR ambient temperature. The temperature data is typically noisy over short timescales, so averaging over short timescales is necessary to effectively apply the correction. Equations 23, 24, and 25 are used to apply the correction.

$$Count_{corr,i} = \begin{cases} Count_i & \text{for } i = 1, 2, 3, \dots, n \\ Count_i - A(T_{sm,i} - T_{ave}) & \text{for } i = n + 1, n + 2, \dots, N \end{cases} \quad (23)$$

$$T_{ave} = \frac{1}{n} \sum_{i=1}^n T_i \quad (24)$$

$$T_{sm,i} = \frac{1}{n} \sum_{j=i-n}^i T_j \quad (25)$$

where $A = -405$, $Count_{corr,i}$ is the temperature corrected count at point i , $Count_i$ is the measured count at point i , T_{ave} is the mean of the CWVR ambient temperature for the first n seconds of a N -second total observation time, $T_{sm,i}$ is the temperature at point i taken as the mean from the preceding n seconds to point i , and T_j is the measured CWVR ambient temperature at point j . The result of applying temperature correction with $n = 5$ min for Channels 2 is shown in Figure 24, and there is a clear improvement in the large-scale count fluctuations. Channels 3 to 5 show a similar improvement.

5.4.3. Single channel Allan Standard Deviations with temperature correction

The temperature corrected and uncorrected ASDs for Channels 2 for $n = 5, 10$, and 20 min are shown in Figure 25. The results show that while the temperature corrected ASDs are more stable than the uncorrected ASDs at $\tau_{long} = 10^3$ sec, the uncorrected ASDs provide better stability from $\tau \sim 10^{0.8} - 10^{2.6}$

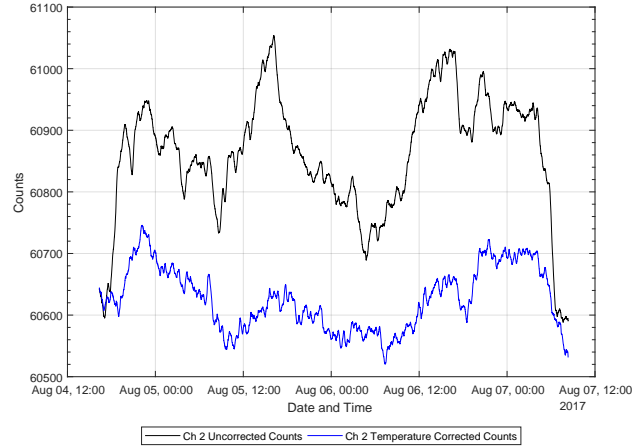


Fig. 24. Channel 2 uncorrected and temperature corrected counts with $n = 5$ min over 64 hr. The plots are averaged with a 20 min running mean.

sec. Temperature averaging time, $n = 5$ min, results in slightly worse gain stability from $\tau \sim 10^{0.8} - 10^{2.65}$ sec but better gain stability at $\tau_{long} = 10^3$ sec than the $n = 10$ and 20 min cases. The results indicate that a temperature averaging time of $n = 10$ min is optimal for stability at both short and long timescales, and the temperature corrected ASDs with $n = 10$ min are $< 2 \times 10^{-4}$ over $\tau = 2.5 - 10^3$ sec, which meet the requirement. Channels 3 to 5 show a similar improvement.

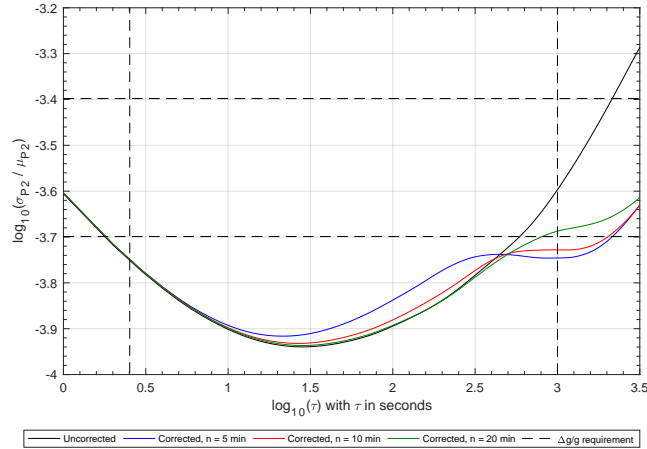


Fig. 25. Channel 2 Temperature Corrected Allan Standard Deviations for $n = 5, 10$, and 20 min.

5.4.4. Observable Allan Standard Deviation with temperature correction

The temperature corrected and uncorrected ASDs of the observable for $n = 5, 10$, and 20 min are shown in Figure 26. The results show that for a temperature averaging time of $n = 10$ min, the temperature corrected ASD is unaffected from $\tau = 10^{0.4} - 10^{2.4}$ sec and improves from $\tau = 10^{2.4} - 10^3$ sec compared to the uncorrected ASD. Therefore, it is recommended that $n = 10$ min be used as the optimum temperature averaging time for temperature correction of the output counts.

6. Summary

The compact water vapor radiometer (CWVR) was characterized in the laboratory, and results show that the design meets the dynamic range, channel isolation, and gain stability requirements to be tested on an

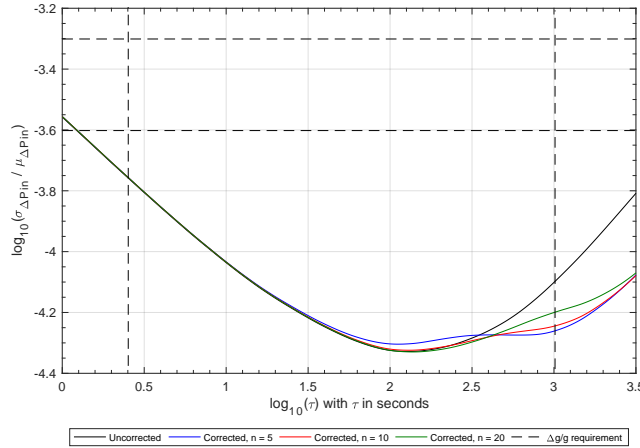


Fig. 26. Observable ΔP_{in} temperature corrected Allan Standard Deviation for $n = 5, 10$, and 20 min.

antenna. The channel isolation requirement of < -20 dB was met, indicating $< 1\%$ power leakage between any two channels. Channel 1 needs to be repaired. The fluctuations in output counts are negatively correlated to the CWVR ambient temperature, with a change of ~ 405 counts per 1°C change in temperature. With temperature correction, the single channel and channel difference gain stability is $< 2 \times 10^{-4}$, and the observable gain stability is $< 2.5 \times 10^{-4}$ over $\tau = 2.5 - 10^3$ sec, all of which meet the gain stability requirement. Future work consists of building more CWVRs and testing the phase correlations on the VLA antennas to evaluate the use of WVR for not only the VLA, but also the Next Generation Very Large Array (ngVLA).

Acknowledgments

This work was possible through the National Radio Astronomy Observatory Graduate Student Research Assistantship program. I would like to thank R. Selina, B. Butler, R. Perley, J. Jackson, W. Grammer, and B. Willoughby for their guidance and support, C. Hennies for his assistance with the hardware, W. Koski for his assistance with the F318 module, the monitor and control system, and the 10 Hz calibration signal, G. Peck for the VHDL code, H. Frej for his assistance with the software, D. Urbain for his assistance with the K-band Dewar setup for the stability tests, and M. Morgan for the MMIC design. The National Radio Astronomy Observatory is a facility of the National Science Foundation operated under cooperative agreement by Associated Universities, Inc.

References

- Butler, B. [1999] *Some Issues for Water Vapor Radiometry at the VLA*, VLA Scientific Memo # 177.
- Carilli, C. L & Holdaway, M. A. [1999] *Tropospheric phase calibration in millimeter interferometry*, *Radio Science*, vol. 34, no. 4, pp. 817-810.
- Chandler, C. J, Briskin, W. F, Butler, B. J, Hayward, R. H, M., Willoughby, B. E. [2004] *Results of Water Vapor Radiometry Tests at the VLA*, EVLA Memo # 73.
- Chandler, C. J, Briskin, W. F, Butler, B. J, Hayward, R. H, Morgan, M., Willoughby, B. E. [2004] *A Proposal to Design and Implement a Compact Water Vapor Radiometer for the EVLA*, EVLA Memo # 74.
- Clark, B. [2015] *Calibration Strategies for the Next Generation VLA*, ngVLA Memo # 2.
- Cornwell, T. J., and Fomalont, E. [1999] *Aperture Synthesis in Radio Astronomy II*, edited by Taylor, G., Carilli, C., & Perley, R., pp. 187-199, *Astron. Soc. of the Pac.*, San Francisco, Calif.
- Desai, K. [1993] *Measurement of turbulence in the interstellar medium*, Ph.D. thesis, 89 pp., Univ. of Calif. at Santa Barbara.
- Dicke, R. H., Beringer, R., Kyhl, R. L., and Vane, A. B. [1946] *Atmospheric absorption measurements with a microwave radiometer*, *Phys. Rev.*, 70, pp. 340-348.
- Fomalont, E., and Perley, R. A. [1999] *Aperture Synthesis in Radio Astronomy II*, edited by Taylor, G., Carilli, C., and Perley, R. A. pp. 79-109, *Astron. Soc. of the Pac.*, San Francisco, Calif.

- Holdaway, M. A. [1992] *Possible phase calibration schemes for the MMA*, Millimeter Array Memo. 84, pp. 14.
- Holdaway, M. A., and Owen F. N. [1995] *A test of fast switching phase calibration with the VLA at 22GHz*, Millimeter Array Memo. 126, pp. 8.
- Koski, W. M. [2017] *F318 WVR & Low-Band Interface Module*, EVLA Front End Group, Document # A23185N0044, Revision B.
- Lay, O. P. [1997] *Phase calibration and water vapor radiometry for millimeter-wave arrays*, *Astron. Astrophys. Suppl. Ser.*, 122, pp. 547-565.
- Sterling, A., Hills, R., Richer, J., Pardo, J. [2004] *183 GHz water vapour radiometers for ALMA: Estimation of phase errors under varying atmospheric conditions*, ALMA Memo # 496.
- Sutton, E. C., and Hueckstaedt, R. M. [1997] *Radiometric monitoring of atmospheric water vapor as it pertains to phase correction in millimeter interferometry*, *Astron. Astrophys. Suppl. Ser.*, 119, pp. 559-567.
- Thompson, A. R., Moran, J. M, Swenson Jr., G. W [2001] *Interferometry and Synthesis in Radio Astronomy*, 2nd edition (John Wiley & Sons, New York).